We are IntechOpen,
the world's leading publisher of
Open Access books
Built by scientists, for scientists

4,800
Open access books available

122,000
International authors and editors

135M
Downloads

Our authors are among the

154
Countries delivered to

TOP 1%
most cited scientists

12.2%
Contributors from top 500 universities

BOOK CITATION INDEX *CLARIVATE ANALYTICS* *INDEXED*

WEB OF SCIENCE™

Selection of our books indexed in the Book Citation Index
in Web of Science™ Core Collection (BKCI)

Interested in publishing with us?
Contact book.department@intechopen.com

Numbers displayed above are based on latest data collected.
For more information visit www.intechopen.com

Extended Kalman Filtering for the Modeling and Estimation of ICG Pharmacokinetics in Cancerous Tumors using NIR Measurements

Burak Alacam and Birsen Yazıcı
Rensselaer Polytechnic Institute
NY, USA

1. Introduction

Near infrared (NIR) diffuse optical imaging and spectroscopy methods provide quantitative functional information that cannot be obtained by the conventional radiological methods (Yodh & Chance, 1995; Intes & Chance, 2005; Boas et al., 2001a). NIR techniques can provide *in vivo* measurements of the oxygenation and vascularization states, uptake and release of optical contrast agents, and chromophore concentrations with high sensitivity. In particular, NIR diffuse optical techniques in conjunction with optical contrast agents have the potential to characterize angiogenesis, and to differentiate between malignant and benign tumors (Hawrys & Sevick-Muraca, 2000; Furukawa et al., 1995; Chen et al., 2003; Becker et al., 1997). Among many commercially available optical contrast agents, only indocyanine green (ICG) is approved for human use by the Food and Drug Administration (El Deosky et al., 1999; Hansen et al, 1993; Shinohara et al., 1996). ICG is a blood pooling agent that has different delivery behaviour between normal and cancer vasculature. In normal tissue, ICG acts as a blood flow indicator in tight capillaries of normal vessel. However in tumor, ICG may act as a diffusible (extravascular) flow in leaky capillary of vessels (Alacam et al., 2006; Cuccia et al., 2003; Ntziachristos et al., 2000; Vaupel et al., 1991). Therefore, pharmacokinetics of ICG has the potential to provide new tools for tumor detection, diagnosis, and staging.

A number of research groups reported compartmental modeling of ICG time-kinetic measurements using NIR methods for tumor diagnosis in animal and human subjects (Gurfinkel et al., 2000; Cuccia et al., 2003; Intes et al., 2003; Milstein et al., 2005). A compartmental model is a mathematical description of the concentrations of contrast agents in which each compartment represents a kinetically distinct tissue type (Tornoe, 2002; Anderson, 1983; Cobelli et al., 2000). It consists of a set of coupled ordinary differential equations (ODE) and a measurement model. Coefficients of the ODE's are the physiological parameters of interest that represent rates of exchange between different compartments. These parameters are non-linearly related to the total concentration of ICG measured by NIR methods. Furthermore, concentration of ICG in each compartment cannot be directly measured non-invasively by NIR techniques, making the pharmacokinetic parameter estimation a highly non-linear problem.

Current methods of ICG compartmental modeling involve curve fitting methods and various techniques for solving differential equations. Gurfinkel et al. presented a two-

compartment model for ICG kinetics, and estimated model parameters (Gurfinkel et al., 2000). The measurements were obtained using a frequency domain photon migration system coupled with a charge-coupled device. The pharmacokinetic parameters were estimated for each pixel based on a curve fitting method. This study indicated that model parameters show no difference in the ICG uptake rates between normal and diseased tissue. Cuccia et al. presented a study of the dynamics of ICG in an adenocarcinoma rat tumor model (Cuccia et al., 2003). A two-compartment model describing the ICG dynamics was used to quantify physiologic parameters related to capillary permeability. The ICG concentration curves were fitted to the compartmental model using a non-linear least squares Levenberg-Marquart algorithm. It was shown that different tumor types have different capillary permeability rates. Intes et al. presented the uptake of ICG by breast tumors using a continuous wave diffuse optical tomography apparatus (Intes et al., 2003). A two-compartment model was used to analyze the pharmacokinetics of ICG. A curve fitting algorithm, namely the non-linear Nelder-Mead simplex search, was used to estimate the pharmacokinetic parameters. This study showed that the malignant cases exhibit slower rate constants (uptake and outflow) as compared to healthy tissue. Milstein et al. presented a Bayesian tomographic image reconstruction method to form pharmacokinetic-rate images of optical fluorophores based on fluorescence diffuse optical tomography (Milstein et al., 2005). Numerical simulations show that the method provides good contrast. However, no real data experiments were presented to study the diagnostic value of spatially resolved pharmacokinetic-rates.

While the studies described above demonstrate the feasibility of the ICG pharmacokinetics in tumor characterization; due to the highly non-linear nature of the pharmacokinetic parameter estimation, variation in parameter values from one subject to another, and sparse data available in clinical and laboratory settings, a systematic and robust approach is needed to model, estimate and analyze ICG pharmacokinetics.

In this chapter, we first present a two-compartmental model for the ICG pharmacokinetics in cancerous tumors. The model captures the transportation of ICG between the vascular and extravascular compartments. We next introduce an extended Kalman filtering (EKF) framework for the estimation of pharmacokinetic-rate parameters and the ICG concentrations in different compartments. The EKF offers a recursive estimation framework with numerous advantages for ICG pharmacokinetic modeling. These include: i) effective modeling of multiple compartments, and multiple measurement systems governed by coupled ordinary differential equations, in the presence of measurement noise and uncertainties in the compartmental model dynamics; ii) simultaneous estimation of pharmacokinetic model parameters and ICG concentrations in each compartment, which are not accessible *in vivo* by means of NIR techniques; iii) recursive estimation of time-varying pharmacokinetic model parameters; iv) statistical validation of estimated concentrations and error bounds on the pharmacokinetic parameter estimates; v) incorporation of available a priori information about the initial conditions of the permeability rates into the estimation procedure; vi) potential real-time monitoring of ICG pharmacokinetic parameters and ICG concentrations in different compartments due to the recursive nature of the EKF estimation method.

We tested our approach using the ICG concentration data acquired from four Fisher rats carrying adenocarcinoma tumor cells. The two-compartment model, composed of plasma and extracellular-extravascular space (EES), was fitted to the data, and pharmacokinetic

Extended Kalman Filtering for the Modeling and Estimation of ICG Pharmacokinetics
in Cancerous Tumors using NIR Measurements
183

model parameters and concentrations in different compartments were estimated using the EKF framework. We then used the model parameters to differentiate between two types of cancerous tumors. Our study suggests that the permeability rates out of the vasculature are higher in edematous tumors as compared to necrotic tumors. Additionally, we observe that in the two-compartment model, the ICG concentration curve is higher in the EES compartment in edematous tumors.

Next, we describe a method of forming pharmacokinetic-rate images, and present spatially resolved pharmacokinetic-rates of ICG using *in vivo* NIR data acquired from three patients with breast tumors. We first reconstructed a set of spatio-temporally resolved ICG concentration images based on differential diffuse optical tomography (Ntziachristos et al., 1999). We modeled the ICG pharmacokinetics by the two-compartment model. Next, we estimated the ICG pharmacokinetic-rates and the concentrations in different compartments based on the EKF framework. The pharmacokinetic-rate images show that the rates from the tumor region and outside the tumor region are statistically different.

The chapter is organized as follows: In Section 2, we present the two-compartment model for the ICG pharmacokinetics in tissue, and the state-space representation of the compartmental model. In Section 3, we introduce the EKF framework for the estimation of ICG pharmacokinetics. In Section 4, we present the estimation of ICG pharmacokinetics in Fischer rat data. In Section 5, we present the reconstruction of ICG pharmacokinetic-rate images using the EKF framework; and the spatially resolved ICG pharmacokinetic-rate images from *in vivo* breast data. Finally, we summarize the Chapter in Section 6.

2. Pharmacokinetic modeling of ICG

2.1 Indocyanine green

ICG is an optical dye commonly used in retinopathy and hepatic diagnostics. Given its low toxicity and FDA approval, it has recently been utilized as a blood pooling agent for the detection and diagnosis of cancerous tumors by means of NIR optical methods. The absorption peak of ICG is 805 nm and the fluorescence peak is at 830 nm. ICG has strong affinity for blood proteins. In plasma, ICG is near-completely bound, primarily to albumin. As a result, its *in vivo* kinetics is similar to those of a 70 kD molecule, although it has a molecular weight of about 700 D (Hansen et al., 1993; Shinohara et al,. 1996; ElDeosky et al., 1999; Li et al., 1995, Yates et al., 1983).

ICG is eliminated from the body primarily through the bile. Outside of the circulatory system, it is not available for removal until it returns to the system. The kinetics of this transition offers a potential means of non-invasively assessing the leakiness of large molecules from the microvasculature; this permeability is a characteristic of the poorly developed vasculature observed in angiogenesis. The increase in local microvasculature density is also expected to induce increased perturbation in the optical signal from intercapillary ICG.

There are some differences in the delivery of ICG between normal and cancerous vasculature. In normal tissue, ICG acts as a blood flow indicator in tight capillaries of normal vessels. However in tumors, ICG may act as a diffusible (extravascular) flow in the leaky capillary of cancer vessels. To investigate the validity of this hypothesis, one has to employ at least a two-compartment model composed of plasma and EES. Additionally, the permeability rate is expected to increase as the malignancy advances (Alacam et al., 2006;

Cuccia et al., 2003; Intes et al., 2003). Fig. 1 (a) and (b) illustrates the ICG flow for healthy and malignant tissue, respectively.
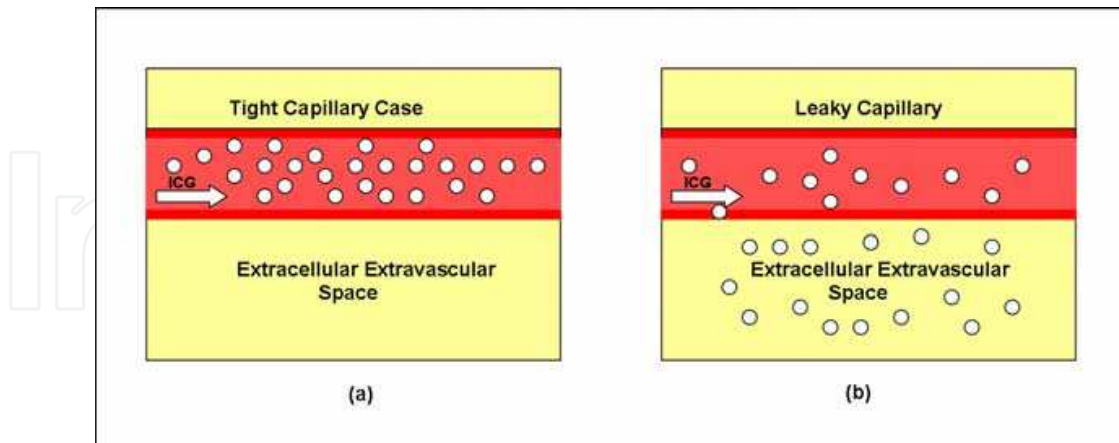

Fig. 1. An illustration of the ICG flow (a) in tight capillary of normal vessel, (b) in permeable capillary of tumor tissue.

2.2 Two-compartment model for the ICG pharmacokinetics

Compartmental modeling allows relatively simple and effective mathematical representation of complex biological responses due to contrast agents and drugs. A region of interest is assumed to consist of a number of compartments, generally representing a volume or a group of similar tissues into which the contrast agent is distributed. The concentration change in a specific compartment is modeled as a result of the exchange of contrast agent between connected compartments. These changes are modeled by a collection of coupled ODEs; each equation describing the time change dictated by the biological laws that govern the concentration exchanges between the interacting compartments (Tornoe, 2002; Anderson, 1983; Jacquez, 1972; Cobelli et al., 2000).

In Alacam et al 2006, we presented 3 different compartment models for the ICG pharmacokinetics and determined that the optimal model is the two-compartment model using the Bayesian information criteria (BIC) (Schwarz, 1978; Box et al., 1994; Akaike, 1980). In order to calculate the BIC for different compartmental models, we first derived a likelihood function for the EKF. The derivation is based on maximum likelihood estimation of the parameters in the Kalman filtering framework given as in (Harvey, 1993; Sallas & Harville, 1988). In the two-compartment model, the tumor region is assumed to be composed of plasma and the EES compartments (Alacam et al., 2006; Tofts et al., 1999; Tofts, 1997; Cuccia et al., 2003). The EES is defined as the region that lies outside of both the vascular region and the tumor cells. We consider transcapillary leakage to occur only at the tumor site. We also assume that a small perturbation of the global plasma concentration does not affect the bulk removal. Fig. 2 shows the block diagram of the two-compartment model for the ICG pharmacokinetics.

Let C_p and C_e denote the ICG concentrations in plasma and the EES, respectively. Then the two-compartment ICG chemical transport equations are given as follows:

The leakage into and the drainage out of plasma:

$$\frac{dC_p(t)}{dt} = k_b C_e(t) - k_a C_p(t) - k_{out} C_p(t) \tag{1}$$

Extended Kalman Filtering for the Modeling and Estimation of ICG Pharmacokinetics
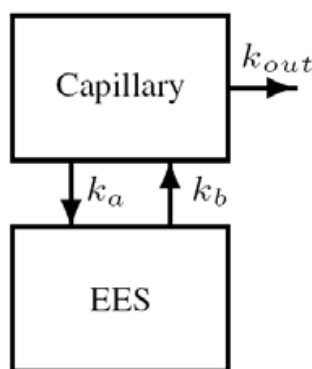in Cancerous Tumors using NIR Measurements

185

Fig. 2. Block diagram of the two-compartment model for ICG pharmacokinetics.

The leakage into and the drainage out of the EES:

$$\frac{dC_e(t)}{dt} = k_a C_p(t) - k_b C_e(t) \tag{2}$$

The parameters k_a and k_b govern the leakage into and the drainage out of the EES, respectively. The parameter k_{out} describes the ICG elimination from the body through kidneys and liver.

Actual bulk ICG concentration in the tissue measured by NIR is a linear combination of plasma and EES ICG concentrations given by:

$$m(t) = v_p C_p(t) + v_e C_e(t) \tag{3}$$

where the parameters v_p and v_e denote plasma and the EES volume fractions, respectively.

3. Extended Kalman filtering for the ICG pharmacokinetics

For the rest of the chapter, all matrices and vectors are denoted in boldface and scalar quantities are denoted in non-boldface notation.

3.1 State-space representation of the ICG pharmacokinetics

Coupled differential equations resulting from the two-compartment modeling of the ICG pharmacokinetics can be expressed in state-space representation as follows:

$$
\begin{bmatrix} dC_e(t) \\ dC_p(t) \end{bmatrix} = \begin{bmatrix} -k_b & k_a \\ k_b & -(k_a + k_{out}) \end{bmatrix} \begin{bmatrix} C_e(t) \\ C_p(t) \end{bmatrix} + d\mathbf{B}(t)
$$
$$
m(t) = \begin{bmatrix} v_e & v_p \end{bmatrix} \begin{bmatrix} C_e(t) \\ C_p(t) \end{bmatrix} + \eta(t)
\tag{4}
$$

where $dB(t)$ is the Weiner process increment, $d\mathbf{B}(t) = \omega(t)dt$. Here, $\omega(t)$ and $\eta(t)$ can be thought of as uncorrelated zero mean Gaussian process with covariance matrix Q, and variance σ^2, respectively.

In vector-matrix notation, the continuous time state-space representation for the n-compartment model is given by:

$$dC(t) = \kappa(\alpha)C(t)dt + dB(t)$$
$$m(t) = V(\alpha)C(t) + \eta(t)$$
(5)

In Equation (5), $C(t)$ denotes the concentration vector; α is the parameter vector whose elements are the pharmacokinetic rates and the volume fractions; $\kappa(\alpha)$ is the system matrix; and $V(\alpha)$ is the measurement matrix. For example the parameter vector α for the two-compartment model is given by

$$\alpha = \begin{bmatrix} k_a & k_b & k_{out} & v_e & v_p \end{bmatrix}$$
(6)

The ICG measurements in Equation (5) are collected at discrete time instances, $t=kT$, k=0,1, ..., where T is the sampling period. Therefore, the continuous model described in Equation (14) has to be discretized. To simplify our notation, we shall use $C(k) = C(kT)$ and $m(k) = m(kT)$. The discrete state space system and the measurement models are given as follows:

$$C(k+1) = \kappa_d(\alpha)C(k) + \omega(k)$$
$$m(k) = V_d(\alpha)C(k) + \eta(k)$$
(7)

where $\kappa_d(\alpha) = e^{\kappa(\alpha)T}$ is the discrete-time system matrix and $V_d(\alpha) = V(\alpha)$ is the discrete-time measurement matrix. $\omega(k)$ and $\eta(k)$ are zero mean Gaussian white noise processes with covariance matrix Q_d and variance σ_d^2, respectively. Discretization of state-space models can be found in various system theory books, see for example (Chen, 1999)

An explicit form of the discrete state space model for the two-compartment case is given as follows:

$$\begin{bmatrix} C_e(k+1) \\ C_p(k+1) \end{bmatrix} = \begin{bmatrix} \tau_{11} & \tau_{12} \\ \tau_{21} & \tau_{22} \end{bmatrix} \begin{bmatrix} C_e(k) \\ C_p(k) \end{bmatrix} + \omega(k)$$
$$m(k) = \begin{bmatrix} v_e & v_p \end{bmatrix} \begin{bmatrix} C_e(k) \\ C_p(k) \end{bmatrix} + \eta(k)$$
(8)

where τ_{ij} is the ith row and j^{th} column entry of the system matrix $\kappa_d(\alpha)$. Note that the matrix entry is an exponential function of the parameters k_a and k_b and k_{out}. To simplify the estimation process, we shall first estimate the matrix entries, τ_{ij}, and then compute the pharmacokinetic rates for each compartmental model.

3.2 Modeling of ICG pharmacokinetic rates and concentrations as unknown states

The Kalman filter provides a recursive method to estimate the states in state-space models, in which the states are driven by noise, and the measurements are collected in the presence of measurement noise (Zarchan, 2000; Chui & Chen, 1999; Catlin, 1989). In the case of non-linear state-space models, the EKF linearizes the model around the current state estimate, and then applies the KF to the resulting linear model. The EKF framework is also utilized for the joint estimation of the unknown system and/or measurement parameters and states. In a linear state-space model when both states and system parameters are unknown, the linear state-space model can be regarded as a non-linear model in which the linear system

Extended Kalman Filtering for the Modeling and Estimation of ICG Pharmacokinetics
in Cancerous Tumors using NIR Measurements
187

parameters and states are combined to form the new states of the non-linear model. This system is then linearized and solved for the unknown states using the KF estimator. We consider a linear Taylor approximation of the non-linear model. The details of the linearization procedure and a general discussion on EKF can be found in (Chui & Chen, 1999; Lyung, 1979; Togneri & Deng, 2003; Nelson & Stear, 1976).

In our problem, the objective is to simultaneously estimate the states, i.e., the ICG concentrations in each compartment, and the system and measurement parameters, i.e., the pharmacokinetic parameters and the volume fractions. Let $\boldsymbol{\theta}$ denote the discrete-time parameter vector of the pharmacokinetic rates and volume fractions. For example, in the two-compartment model, $\boldsymbol{\theta}$ is given by

$$\boldsymbol{\theta} = \begin{bmatrix} \tau_{11} & \tau_{12} & \tau_{21} & \tau_{22} & v_e & v_p \end{bmatrix} \tag{9}$$

In order to estimate $\boldsymbol{\theta}$ within the EKF framework, the following dynamic model is introduced:

$$\boldsymbol{\theta}(k+1) = \boldsymbol{\theta}(k) + \boldsymbol{\zeta}(k) \tag{10}$$

where $\boldsymbol{\zeta}(k)$ is a zero mean white noise process with covariance matrix S_d (Chui and Chen, 1999). Here, $\boldsymbol{\theta}(k)$ can be thought of as the kth update of the parameter rather than its value at time k.

We append the parameter vector $\boldsymbol{\theta}(k+1)$ to the ICG concentration vector $\mathbf{C}(k+1)$ to form the new non-linear state-space model given by

$$\begin{bmatrix} \mathbf{C}(k+1) \\ \boldsymbol{\theta}(k+1) \end{bmatrix} = \begin{bmatrix} \mathbf{K}(\boldsymbol{\theta})\mathbf{C}(k) \\ \boldsymbol{\theta}(k) \end{bmatrix} + \begin{bmatrix} \boldsymbol{\omega}(k) \\ \boldsymbol{\zeta}(k) \end{bmatrix}$$

$$m(k) = \begin{bmatrix} V_d(\boldsymbol{\theta}) & 0 \end{bmatrix} \begin{bmatrix} \mathbf{C}(k) \\ \boldsymbol{\theta}(k) \end{bmatrix} + \eta(k) \tag{11}$$

where $\mathbf{K}(\boldsymbol{\theta}) = \boldsymbol{\kappa}_d(\boldsymbol{\alpha})$.

3.3 Joint estimation of ICG concentrations, pharmacokinetic parameters, and volume fractions within EKF framework

In this section we will summarize the major steps of the EKF estimator for the joint estimation of ICG concentrations and compartmental model parameters. Let the subscript $k \,|\, t$ denote the estimate at time k given all the measurements up to time t. Then the 1-step ahead prediction of the ICG concentrations and the compartmental model parameters are given as follows:

$$\begin{bmatrix} \hat{\mathbf{C}} \\ \hat{\boldsymbol{\theta}} \end{bmatrix}_{k|k-1} = \begin{bmatrix} \mathbf{K}(\hat{\boldsymbol{\theta}})\hat{\mathbf{C}} \\ \hat{\boldsymbol{\theta}} \end{bmatrix}_{k-1|k-1} \tag{12}$$

For the two-compartment model, Equation (12) becomes

$$\begin{bmatrix} \hat{C}_e \\ \hat{C}_p \\ \hat{\boldsymbol{\theta}} \end{bmatrix} = \begin{bmatrix} \hat{\tau}_{11}\hat{C}_e + \hat{\tau}_{12}\hat{C}_p \\ \hat{\tau}_{21}\hat{C}_e + \hat{\tau}_{22}\hat{C}_p \end{bmatrix}_{k-1|k-1} \tag{13}$$

The error covariance matrix, $\mathbf{P}_{k|k-1}$, of the 1-step ahead predictions is given as follows:

$$\mathbf{P}_{k|k-1=}\mathbf{J}_{k-1}\mathbf{P}_{k-1|k-1}\mathbf{J}_{k-1}^{T} + \begin{bmatrix} \mathbf{Q}_d & 0 \\ 0 & \mathbf{S}_d \end{bmatrix} \tag{14}$$

where $\mathbf{J}_k$ is the Jacobian of the non-linear EKF system function at time k. Explicitly, it is given by:

$$\mathbf{J}_k = \begin{bmatrix} \mathbf{K}(\hat{\boldsymbol{\theta}}) & \dfrac{\partial}{\partial \boldsymbol{\theta}}\Big[\mathbf{K}(\hat{\boldsymbol{\theta}}_n)\hat{\mathbf{C}} \Big] \\ \mathbf{0} & \mathbf{I} \end{bmatrix}_{k|k} \tag{15}$$

where $\mathbf{0}$ and $\mathbf{I}$ denote zero and identity matrices, respectively. The Jacobian matrix for the two-compartment model becomes

$$\mathbf{J}_k = \begin{bmatrix} \begin{pmatrix} \hat{\tau}_{11} & \hat{\tau}_{12} \\ \hat{\tau}_{21} & \hat{\tau}_{22} \end{pmatrix} & \begin{pmatrix} \hat{C}_e & \hat{C}_p & 0 & 0 & 0 & 0 \\ 0 & 0 & \hat{C}_e & \hat{C}_p & 0 & 0 \end{pmatrix} \\ \mathbf{0}_{6\times2} & \mathbf{I}_{6\times6} \end{bmatrix}_{k|k} \tag{16}$$

The 1-step ahead predictions are updated to the kth-step estimates by means of the Kalman gain matrix which are given by

$$\mathbf{G}_k = \mathbf{P}_{k|k-1}\boldsymbol{\Lambda}^T[\boldsymbol{\Lambda}\mathbf{P}_{k|k-1}\boldsymbol{\Lambda}^T + \sigma_k^2]^{-1} \tag{17}$$

where $\boldsymbol{\Lambda}$ is the following vector:

$$\boldsymbol{\Lambda} = \begin{bmatrix} \mathbf{V}_d(\hat{\boldsymbol{\theta}}) & \dfrac{\partial}{\partial \boldsymbol{\theta}_n}\Big[\mathbf{V}_d(\hat{\boldsymbol{\theta}})\hat{\mathbf{C}} \Big] \end{bmatrix}_{k|k-1} \tag{18}$$

For the two-compartment model the $\boldsymbol{\Lambda}$ vector becomes

$$\boldsymbol{\Lambda} = \begin{bmatrix} \hat{v}_e & \hat{v}_p & 0 & 0 & 0 & 0 & \hat{C}_e & \hat{C}_p \end{bmatrix} \tag{19}$$

The kth-step estimate of the concentrations and the parameters are obtained using

$$\begin{bmatrix} \hat{\mathbf{C}} \\ \hat{\boldsymbol{\theta}} \end{bmatrix}_{k|k} = \begin{bmatrix} \hat{\mathbf{C}} \\ \hat{\boldsymbol{\theta}} \end{bmatrix}_{k|k-1} + G_k\left(m(k) - \Big[\mathbf{V}_d(\hat{\boldsymbol{\theta}})\hat{\mathbf{C}} \Big]_{k|k-1} \right) \tag{20}$$

The initialization and the convergence properties of the EKF can be found in (Alacam et al., 2006; Chui and Chen, 1999; Ljung, 1979; La Scala et al., 1996; Boutayeb et al., 1997).

4. Estimation of ICG pharmacokinetics in Fischer rat data

We applied the proposed EKF framework to the pharmacokinetic analysis of ICG data obtained from four Fischer rats with adenocarcinoma. R3230ac adenocarcinoma cells were

Extended Kalman Filtering for the Modeling and Estimation of ICG Pharmacokinetics
in Cancerous Tumors using NIR Measurements

189

injected below the skin into four Fischer rats 3 weeks prior to measurements. The tumor size
for the rats varies in diameter from 5 to 30 mm. Measurements were conducted with a
combined frequency-domain and steady-state optical technique that facilitates rapid
measurement of tissue absorption. Frequency domain measurements were obtained at 674,
800, 849, 898, and 915 nm, modulated at frequencies from 50 to 601 MHz, sweeping a total of
233 frequencies. Tumors were also imaged by use of contrast-enhanced magnetic resonance
imaging and coregistered with the location of the optical probe. In addition, a broadband
continuous wave reflectance measurement spanning the range 650-1000 nm was performed
with a spectrometer. With the reduced-scattering coefficient spectrum and diffusion theory,
the broadband reflectance spectra were converted to absorption coefficient spectra. The
absolute concentration of ICG, together with oxy-hemoglobin, deoxy-hemoglobin, and
water were calculated by using multiple linear regressions of ICG extinction coefficient
spectra to the calculated absorption spectrum at approximately every second for ten
minutes. A detailed discussion of the measurement process and apparatus can be found in
(Bevilacqua et al., 1988; Jacubowski, 2002).

Fig. 3 presents the ICG concentrations from four different rats. Tumors in Rat 1 and 2 are
classified as necrotic because of their low tissue oxy-hemoglobin, low total hemoglobin, and
low gadolinium-diethylene-triamine penta-acetic acid (Gd-DTPA) enhancement levels.
Tumors in Rat 3 and 4 are classified as edematous due to their high water content (Merritt et
al., 2003). It can be observed from Fig. 3 that the necrotic cases display low peak ICG
concentration values and slowly rising slopes unlike the edematous cases with high peak
values and sharp rising slopes.

We estimated the pharmacokinetic rates for the two-compartment model (Alacam et al.,
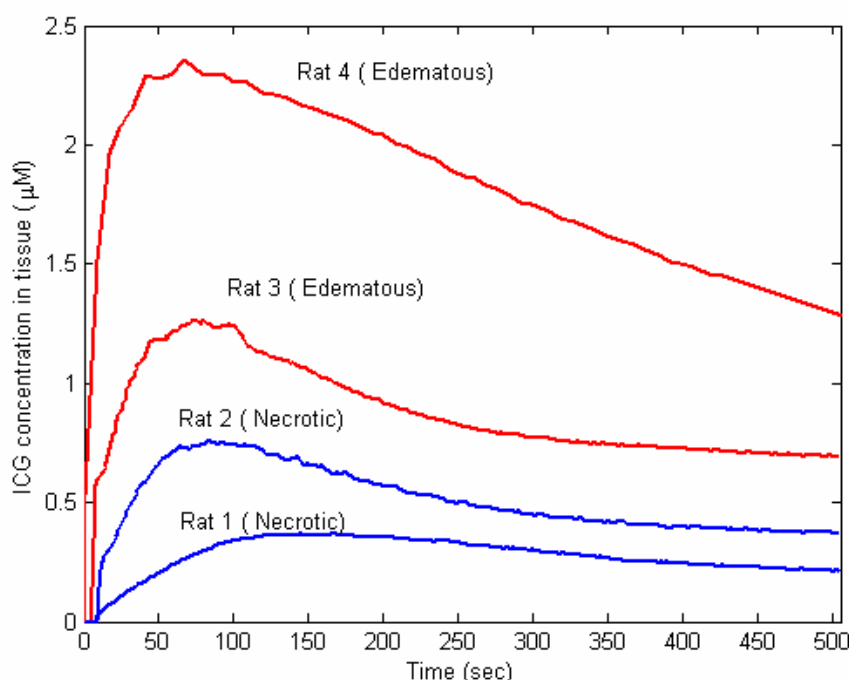2006).

Fig. 3. ICG concentrations measured in tissue for four different rat tumors.

	k_a $(sec^{-1}10^{-2})$	k_b $(sec^{-1}10^{-2})$	k_{out} $(sec^{-1}10^{-3})$	v_e (10^{-2})	v_p (10^{-2})
Rat 1 (Necrotic)	2.47±0.043	1.06±0.052	4.61±0.073	21.8±1.92	1.41±0.053
Rat 2 (Necrotic)	3.54±0.082	2.98±0.086	4.83±0.092	25.4±3.49	2.42±0.088
Rat 3 (Edematous)	6.90±0.101	4.93±0.072	3.95±0.048	30.4±2.81	4.84±0.120
Rat 4 (Edematous)	8.40±0.114	7.77±0.091	4.02±0.068	53.0±4.73	7.03±0.321

Table 1. Estimated pharmacokinetic rates and volume fractions for the two-compartment model.

Table 1 presents the estimated pharmacokinetic rates and volume fractions using the EKF algorithm. The rate of leakage into the EES from the capillary, k_a, range from 0.0247 to 0.0840 1/sec and the rate of drainage out of the EES and into the capillary, k_b, range from 0.0106 to 0.0777 1/sec. Note that the permeability rates for the necrotic cases are lower than the ones observed for the edematous cases. Additionally, the estimated values for the pharmacokinetic rates are much higher than the normal tissue values due to the increased leakiness of the blood vessels around the tumor region (Alacam et al., 2006; Cuccia et al., 2003; Su et al., 1998). The estimated plasma volume fractions agrees with the values reported earlier (Cuccia et al., 2003), and the values presented in the literature (Fishkin et al., 1997; Buckley, 2002). These results confirm that v_p can be large in tumors and that its magnitude varies with respect to the stage of the tumor (Tofts, 1997). The estimated values of the EES volume fraction, v_e, range from 0.218 to 0.53, in agreement with the 0.2 to 0.5 range reported earlier (Tofts et al., 1999). Note that these results are valid only for the ICG pharmacokinetics in tumor cells R3230ac, adenocarcinoma and may not be generalized for other types of contrast agents or tumor types.

Figure 4 shows the estimated ICG concentrations in plasma and the EES compartments for the two-compartment model for Rats 1 to 4. Note that initial estimates of concentrations are noisy due to the limited data used in the recursive EKF estimation. This can be improved by Kalman backward smoothing (Gelb, 1989). The peak values of the plasma concentration, C_p, range from 2.72 μM to 4.28 μM. The absolute value of the concentrations may not be very useful. However, concentration of ICG in a compartment relative to the one in another compartment may provide useful information. We consider the ratio of the peak concentrations in plasma and the EES as a potential parameter to discriminate different tumors. The peak C_p/C_e ratio for Rats 1 to 4 is 0.551, 0.593, 0.787, and 1.151, respectively.

This ratio is higher in edematous cases consistent with the fact that ICG-albumin leaks more into the EES in edematous tumors. Additionally, the ICG concentration in plasma decays faster than the ICG concentration in the EES due to its elimination through the liver and kidneys.

5. Pharmacokinetic-rate images of indocyanine green from *in vivo* breast data

In this section, we present a method of forming pharmacokinetic-rate images, and spatially resolved pharmacokinetic-rates of ICG using *in vivo* NIR data acquired from three patients with breast tumors.
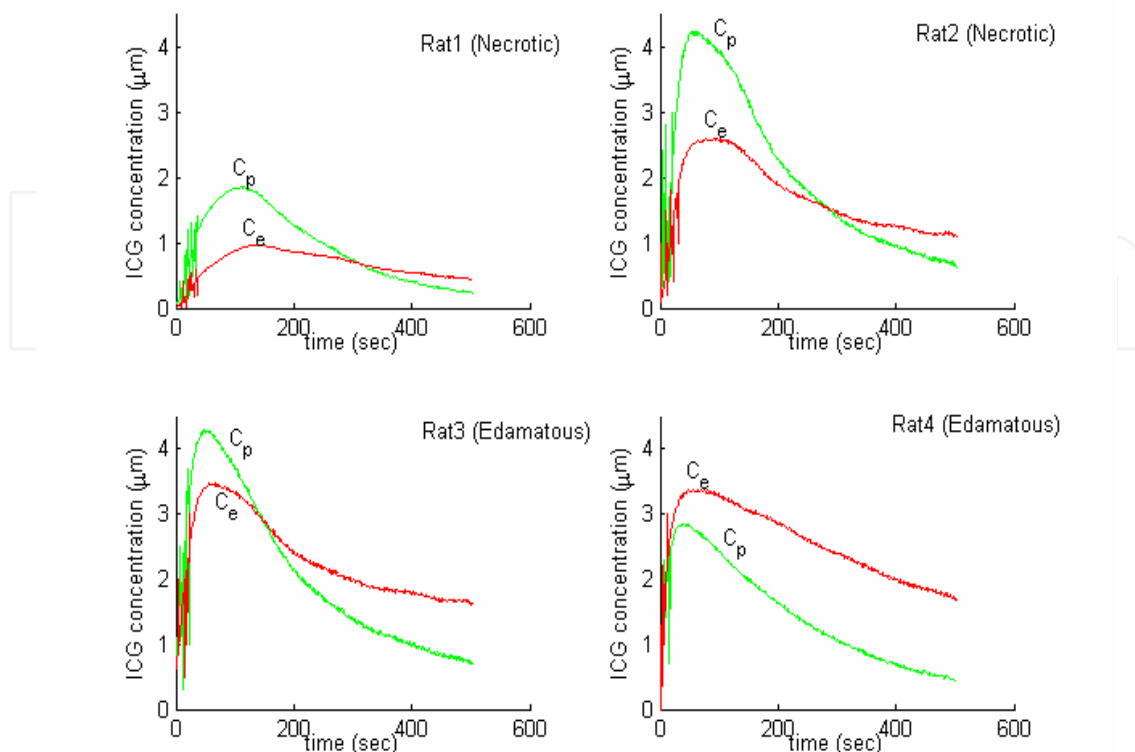
Extended Kalman Filtering for the Modeling and Estimation of ICG Pharmacokinetics
in Cancerous Tumors using NIR Measurements
191

Fig. 4. ICG concentrations in plasma, $C_p(t)$ and EES, $C_e(t)$, for four different rats. (a) Rat1, (b) Rat2, (c) Rat3, and (d) Rat4.

5.1 NIR apparatus and patient information

We used the data collected with a continuous wave (CW) NIR imaging apparatus. The apparatus had 16 light sources, which are tungsten bulbs with less than 1 watt of output power. They were located on a circular holder at an equal distance from each other with 22.5 degrees apart. Sixteen detectors, namely, silicon photodiodes, are situated in the same plane. The breast was arranged in a pendular geometry with the source-detector probes gently touching its surface. The detectors used the same positions as the sources to collect the light originating from one source at a time. Only the signals from the farthest 11 detectors were used in the analysis. A band pass filter at 805 nm, the absorption peak of ICG, was placed in front of the sources to select the desired wavelength. A set of data for one source was collected every 500 ms. Total time for a whole scan of the breast including 16 sources and 16 detectors was about 8.8 seconds. A more detailed explanation of the apparatus and the data collection procedure can be found in (Nioka et al., 1997).

Three different patients with different tumor types were included in the study. Measurements were made before the biopsy to avoid modification of the blood volume and flow in the tumor region. First case, (Case 1), was fibroadenoma, which corresponds to a mass estimated to be 1-2 cm in diameter within a breast of 9 cm diameter located at 6-7 o'clock. Second case, (Case 2), was adenocarcinoma corresponding to a tumor estimated to be 2-3 cm in diameter within a breast of 7.7 cm diameter located at 4-5 o'clock. The third case, (Case 3), was invasive ductal carcinoma, which corresponds to a mass estimated to be 4

by 3 cm located at 6 o'clock. Table 2 describes the tumor information for each patient. *A priori* information on the location and size of the tumor was obtained by palpation and the diagnostic information was derived *a posteriori* from biopsy and surgery. ICG was injected intravenously by bolus with a concentration of 0.25 mg per 1/kg of body weight. Data acquisition started before the injection of ICG and continued for 10 minutes.

	Tumor Type	Tumor Size	Tumor Location
Case 1	Fibroadenoma	1-2 cm	6-7 o'clock
Case 2	Adenocarcinoma	2-3 cm	4-5 o'clock
Case 3	Invasive Ductal Carcinoma	4 by 3 cm	6 o'clock

Table 2. Tumor Information for each patient.

5.2 Reconstruction of bulk ICG concentration images

In our data collection process, a sequence of boundary measurements was collected over a period of time. Each set of measurements was used to form a frame of the ICG concentration images. The resulting sequence of ICG concentration images were then used to form pharmacokinetic-rate images. To reconstruct each frame of the ICG concentration images, we used the differential diffuse optical tomography (DDOT) technique (Alacam et al., 2008, Intes et al., 2003; Ntziachristos et al., 1999).

In DDOT, two sets of excitation measurements are collected corresponding to before and after the ICG injection, and the ICG concentration is determined by the perturbation method (Intes et al., 2003; Ntziachristos et al., 1999). The photon propagation before and after the injection is modeled by the following diffusion equations:

$$\nabla . D_x(r) \nabla \Phi_x^{\pm}(r,\omega) - (\mu_{ax}^{\pm}(r) + j\omega / c) \Phi_x^{\pm}(r,\omega) = 0 \quad r \in \Omega \subset R^3 \quad (21)$$

with Robin-type boundary conditions (Arridge, 1999).

Here *x* stands for the excitation, *c* is the speed of light inside the medium Ω; Ω denotes the modulation frequency of the source, $\mu_{ax}^-(r)$ and $\mu_{ax}^+(r)$ are the absorption coefficients before and after the ICG injection, $D_x(r)$ is the diffusion coefficient which is assumed independent of $\mu_{ax}^{\pm}(r)$, known but not necessarily constant, $\Phi_x^{\pm}(r,\omega)$ denotes optical field at location *r* before and after the ICG injection.

The absorption coefficient after the injection $\mu_{ax}^+(r)$ is modeled as a sum of the absorption coefficient of the medium before the ICG injection $\mu_{ax}^-(r)$ and the perturbation caused by the ICG $\Delta\mu_{ax}(r)$:

$$\Delta\mu_{ax}(r) = \mu_{ax}^+(r) - \mu_{ax}^-(r) \quad\quad r \in \Omega \subset R^3 \quad (22)$$

The forward model, given in Equation (21) is based on the first order Rytov approximation (Intes et al., 2003). We discretize the forward model and relate the relative absorption coefficients of voxels in the imaging volume to Rytov-type measurements by a system of linear equations. Let $\Psi_x(\omega,r_d,r_s)$ denote the Rytov-type measurements at location r_d due to source at r_s. The linearized relationship between the differential absorption coefficient and measurements is given by (O'Leary, 1996)

$$\Psi_x(\omega,r_d,r_s) = -\frac{1}{\Phi_x^-(\omega,r_d,r_s)} \int_\Omega G_x^-(r,\omega;r_d) \Phi_x^-(r,\omega;r_s) \frac{c\Delta\mu_{ax}(r)}{D_x} d^3r \quad (23)$$

Extended Kalman Filtering for the Modeling and Estimation of ICG Pharmacokinetics
in Cancerous Tumors using NIR Measurements
193

where $\Phi_x^-(r,\omega;r_s)$ is the photon density obtained at the excitation wavelength before ICG injection.

$\int_\Omega G_x^-(r,\omega;r_d)$ is the Green's function of Equation (21) for a source at r_s before the injection describing the propagation of light from the heterogeneity r to the detector at r_d.

We approximated the shape of the breast as a cylinder and used the Kirchhoff approximation (Ripoll et al., 2001a; Ripoll et al., 2001b) for diffuse waves to model the interaction of light with boundaries. In order to account for the biological noise, we implemented the forward model with coupling coefficient technique (Boas et al., 2001b).

We addressed the inverse problem of recovering $\Delta\mu_{ax}(r)$ from Rytov-measurements using the singular value decomposition of the Moore-Penrose generalized system. We used a zeroth-order Tikhonov regularization to stabilize the inversion procedure. We applied the L-curve method to an experimental model reconstruction and determined the best regularization parameter using a curvature function as described in (Hansen & O'Leary, 1993). A detailed discussion of the forward and inverse models used for the reconstruction of differential absorption coefficients $\Delta\mu_{ax}(r)$ can be found in (Intes et al., 2003).

To construct a set of ICG concentration images, we used the linear relationship between the differential absorption coefficients and ICG concentrations (Landsman et al., 1976):

$$\Delta\mu_a(r) = \ln 10 \, \varepsilon_\lambda m(r) \tag{24}$$

where ε_λ is the extinction coefficient of ICG at the wavelength 805nm, $m(r)$ is the bulk ICG concentration in the tissue.

Using the method outlined above, we reconstructed a sequence of ICG concentration images. Fig., 5-7 show a set of images reconstructed from *in vivo* breast data for Case 1, 2,
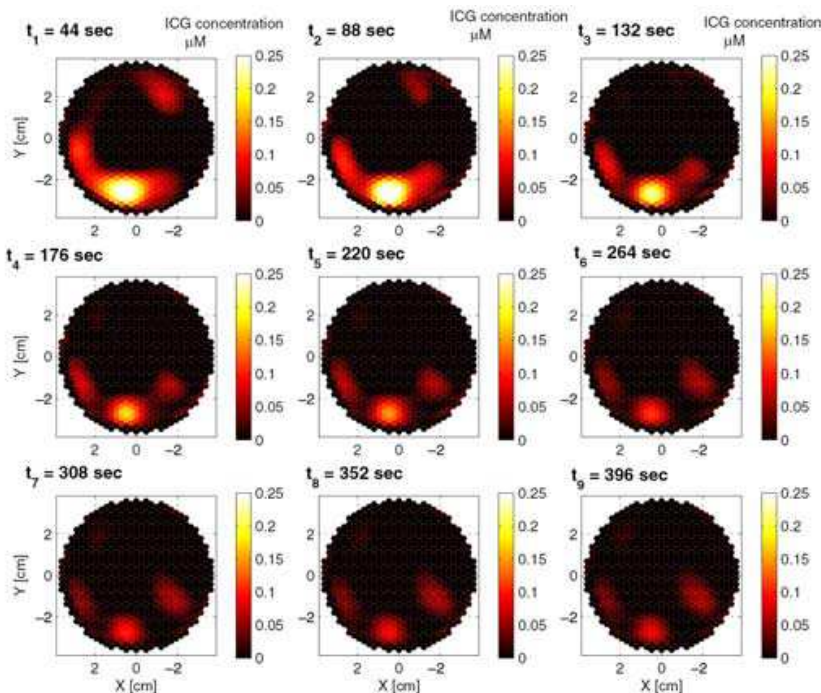

Fig. 5. ICG concentration images for a set of time instants for Case 1.

and 3, respectively. Although only 9 images are displayed, there are approximately 50 images for each case, each corresponding to a different time instant. Each image is composed of 649 voxels. Note that the ICG concentration images in Fig.5-7 represent the bulk ICG concentrations in the tissue, not the ICG concentrations in plasma or the EES compartments.
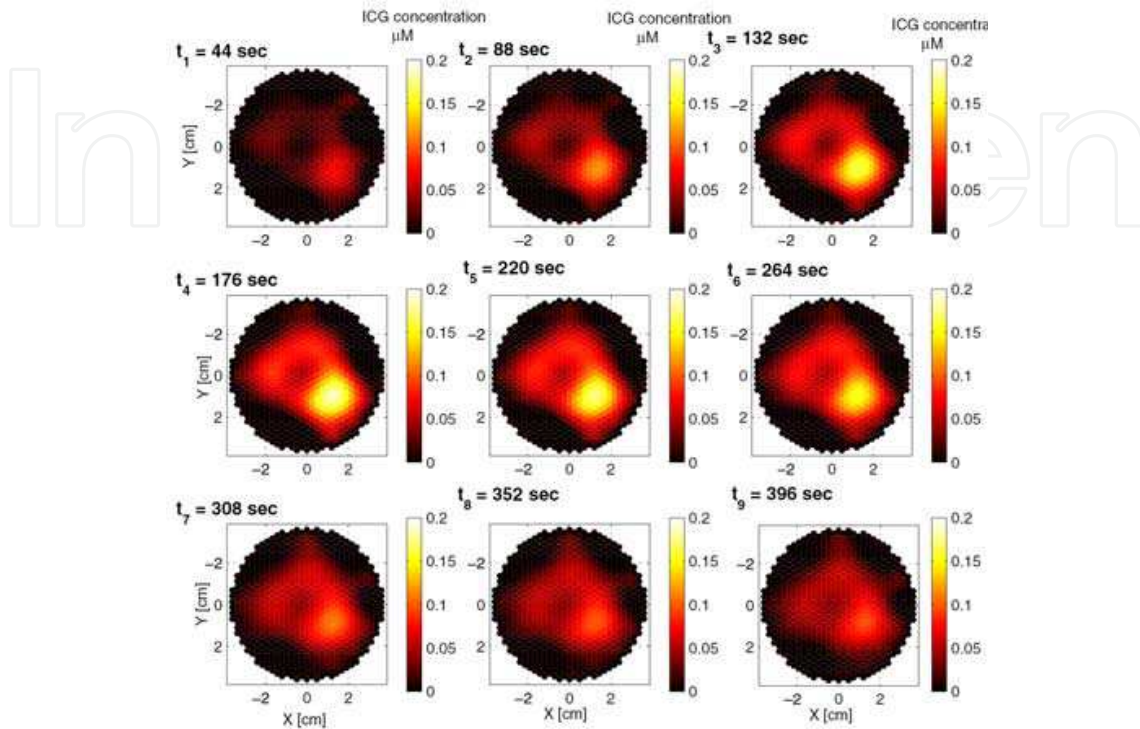

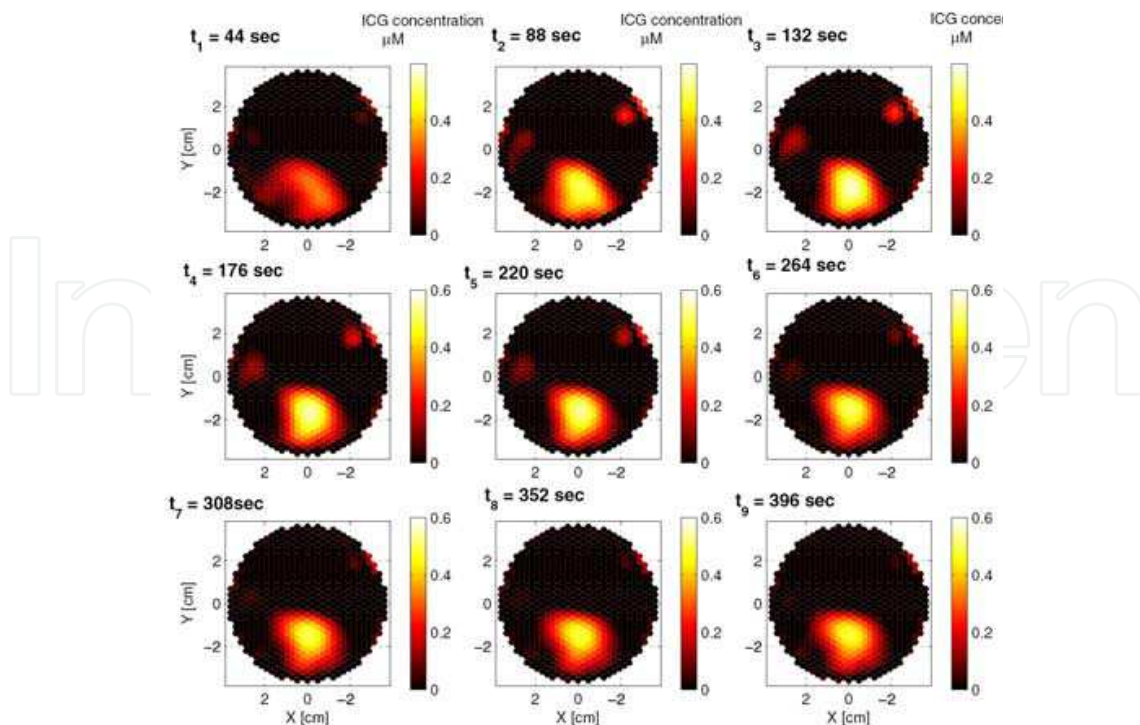Fig. 6. ICG concentration images for a set of time instants for Case 2.

Fig. 7. ICG concentration images for a set of time instants for Case 3.

Extended Kalman Filtering for the Modeling and Estimation of ICG Pharmacokinetics
in Cancerous Tumors using NIR Measurements
195

5.3 Reconstruction of ICG pharmacokinetics from *in vivo* breast data

Our objective is to model the pharmacokinetics of ICG at each voxel of ICG concentration images using the two-compartment model described in Section 2. To do so, we first extracted the time varying ICG concentration curves for each voxel from the sequence of ICG concentration images.

We then fit the two-compartment model to each time course data using the EKF framework; and estimated k_a, k_b, k_{out}, and the ICG concentrations in plasma and the EES. We chose the initial values within the biological limits that lead to minimum norm error covariance matrix for the EKF estimation. The images of k_a, and k_b for each case are shown in Fig. 8(a)-(b), 9(a)-(b), and 10(a)-(b), respectively.
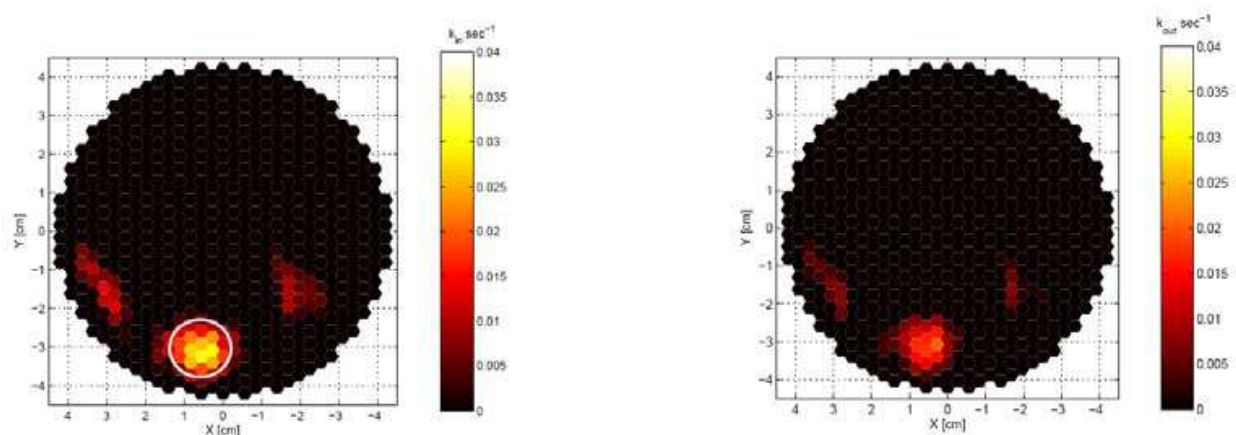
Fig. 8. Pharmacokinetic-rate images, (a) k_a, and (b) k_b for Case 1. The k_a images are shown with approximate tumor location and size.
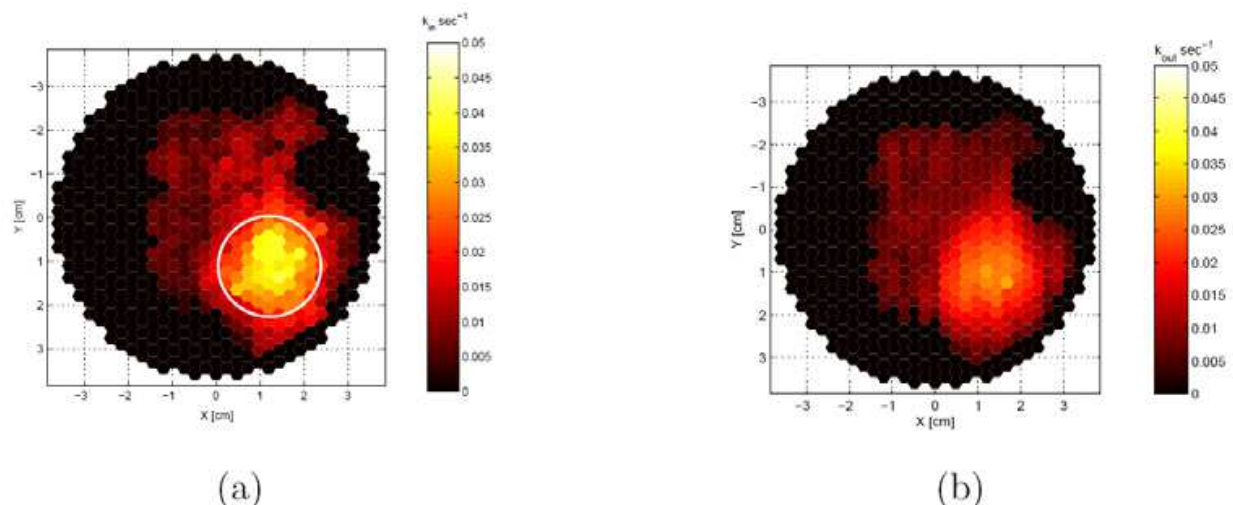
Fig. 9. Pharmacokinetic-rate images, (a) k_a, and (b) k_b for Case 2. The k_a images are shown with approximate tumor location and size.

Using the *a priori* and *a posteriori* information on the location, and the size of the tumors, we plotted an ellipse (or a circle) to identify the approximate location and size of the tumor in the pharmacokinetic-rate images. We note that the radii of the ellipses were chosen large enough to include the tumor boundaries. Fig. 8(a), 9(a), and 10(a) present the k_a images with approximate tumor location and size for Case 1, 2, and 3, respectively. The consistency of
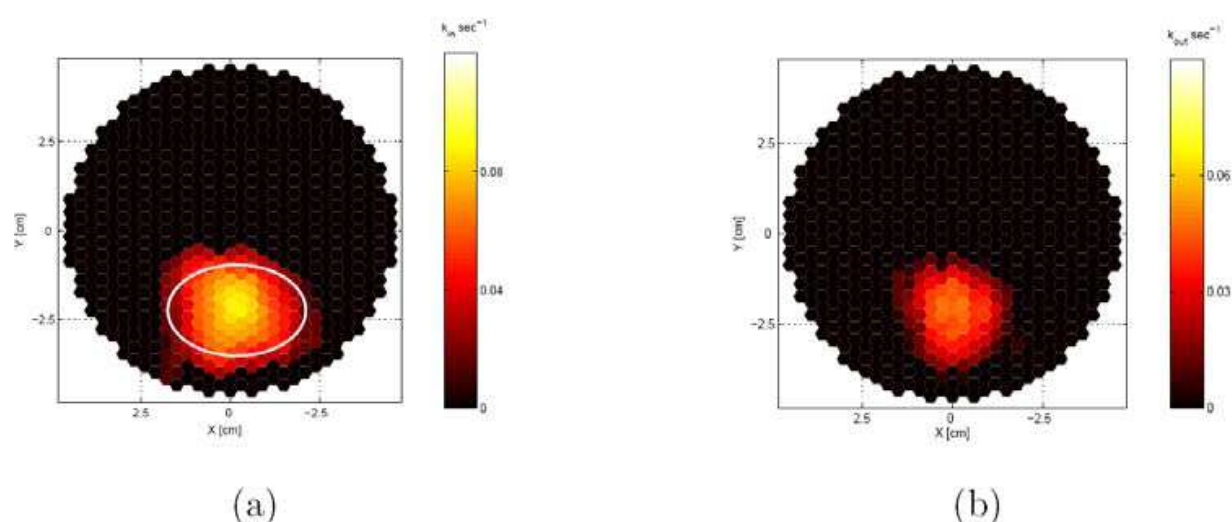
Fig. 10. Pharmacokinetic-rate images, (a) k_a, and (b) k_b for Case 2. The k_a images are shown with approximate tumor location and size.

the bright regions in the k_a images, and circular/elliptical regions drawn based on the *a priori* and *a posteriori* information shows that the pharmacokinetic-rate images may provide good localization of tumors. Table 3 shows the mean values ($\pm$ spatial standard deviation) of the pharmacokinetic-rates for the tumor region and outside the tumor region for all three cases. The pharmacokinetic rates are higher for Case 3 (invasive ductal carcinoma), for both the tumor region and outside the tumor region as compared to Case 2 (adenocarcinoma). Similarly, the kinetic rates are higher for Case 2 (adenocarcinoma), as compared to Case 1 (fibroadenoma) for both the tumor region and outside the tumor region. This observation shows that high mean values of k_a and k_b may be indicative of tumor aggressiveness. Additionally, we constructed the ICG concentration images for plasma and the EES compartments. Figures 11-16 show the ICG concentration in plasma and the EES for 3 different time instants for Case 1, 2, and 3, respectively.

	k_a $(sec^{-1}10^{-2})$		k_b $(sec^{-1}10^{-2})$		k_{out} $(sec^{-1}10^{-3})$	
	Inside	Outside	Inside	Outside	Inside	Outside
Case 1	2.14±0.018	0.73±0.011	1.24±0.069	0.43±0.013	4.11±0.057	3.87±0.012
Case 2	2.92±0.076	1.14±0.052	1.58±0.051	0.65±0.036	3.94±0.081	4.12±0.047
Case 3	6.87±0.093	3.06±0.015	4.96±0.048	1.66±0.072	4.49±0.056	4.46±0.081

Table 3. Mean and standard deviation of pharmacokinetic-rates for the tumor region and outside the tumor region

Our results show that the pharmacokinetic-rates are higher around the tumor region agreeing with the fact that permeability increases around the tumor region due to compromised capillaries of tumor vessels. We also observed that ICG concentrations in plasma and the EES compartments are higher around the tumors agreeing with the hypothesis that around the tumor region ICG may act as a diffusible extravascular flow in leaky capillary of tumor vessels.

Extended Kalman Filtering for the Modeling and Estimation of ICG Pharmacokinetics
in Cancerous Tumors using NIR Measurements
197

6. Conclusion

We presented a two- compartmental model, and an EKF framework for (i) the estimation of bulk ICG pharmacokinetics and (ii) the reconstruction of ICG pharmacokinetic-rate images and concentration images in different compartments. We tested our approach in data obtained from Fischer rats with adenocarcinoma cells and estimated pharmacokinetic rates and volume fractions. The estimated parameters indicate that the permeability rates are higher for edematous cases as compared to the necrotic tumors.

We also presented pharmacokinetic-rate images of ICG using the *in vivo* data acquired from three patients with breast tumors. To form pharmacokinetic-rate images, we used the differential diffuse optical tomography technique. Along with the pharmacokinetic-rates, we also reconstructed the ICG concentration images in plasma and EES compartments. The ICG concentration images in plasma and the EES compartments show that the concentration of ICG is higher in the tumor region agreeing with the hypothesis that around the tumor region ICG may act as a diffusible extravascular flow in leaky capillary of tumor vessels.

While the two-compartment model is sufficient to model the ICG pharmacokinetics, higher-order compartmental models may be advantageous for modeling the pharmacokinetics of functionalized optical contrast agents that actively accumulate or activate in diseased tissue. In the future, we plan to apply higher order compartmental models and the EFK framework to estimate the pharmacokinetics of newly developed optical fluorophores approved for human and/or animal use.
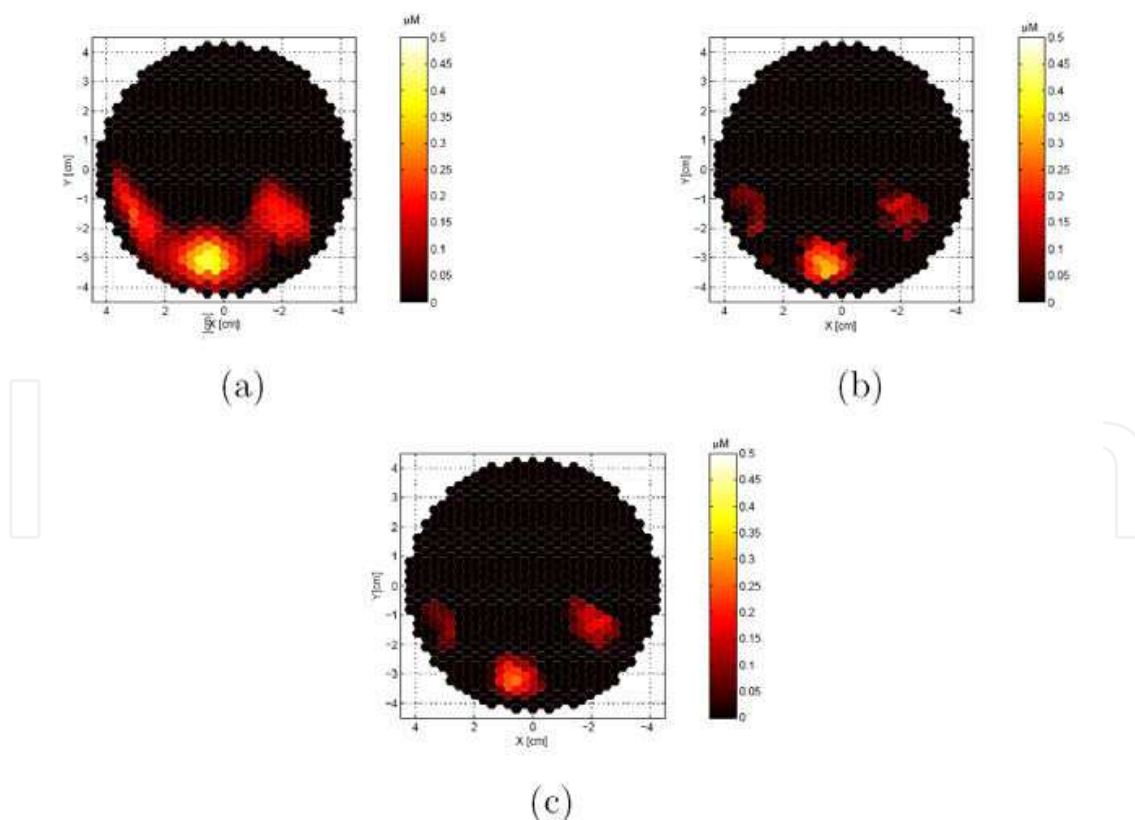

Fig. 11. ICG concentration images in plasma for Case 1 for (a) 246.4th, (b) 334.4th, and (c) 422.4th seconds.
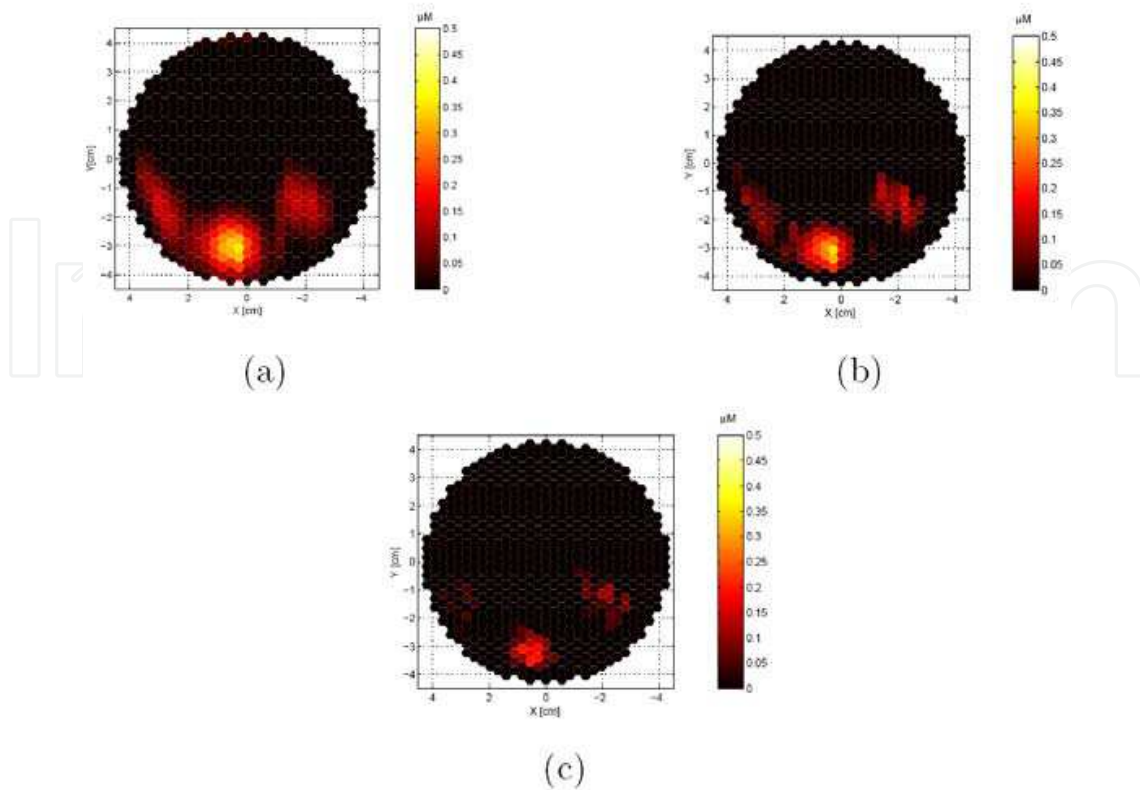
Fig. 12. ICG concentration images in the EES for Case 1 for (a) 246.4th, (b) 334.4th, and (c) 422.4th seconds.
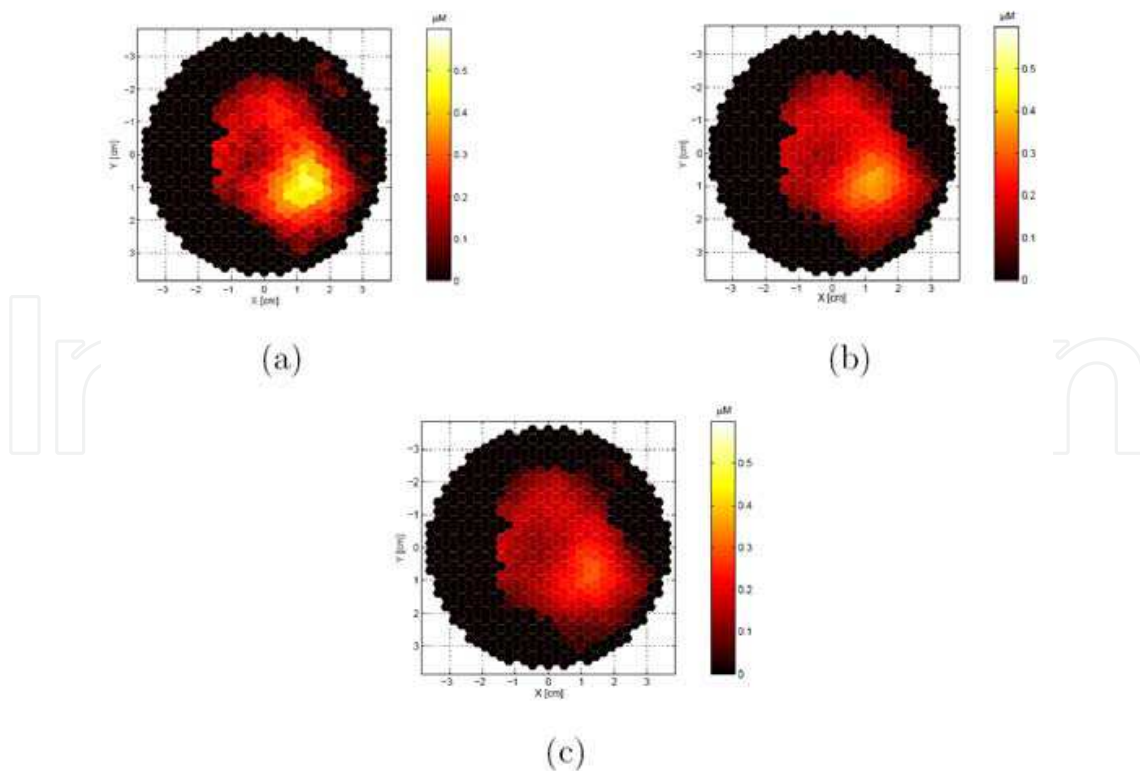

Fig. 13. ICG concentration images in plasma for Case 2 for (a) 228.8th, (b) 316.8th, and (c) 404.8th seconds.
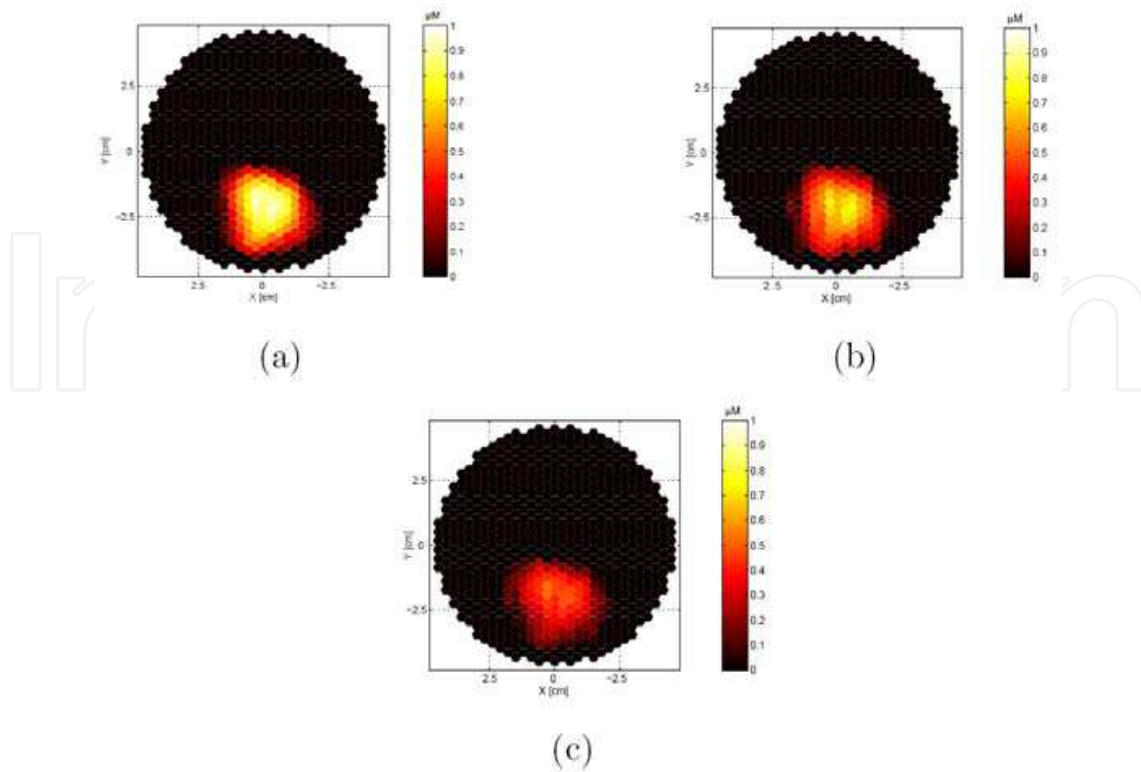
Fig. 14. ICG concentration images in the EES for Case 2 for (a) 228.8th, (b) 316.8th, and (c) 404.8th seconds.
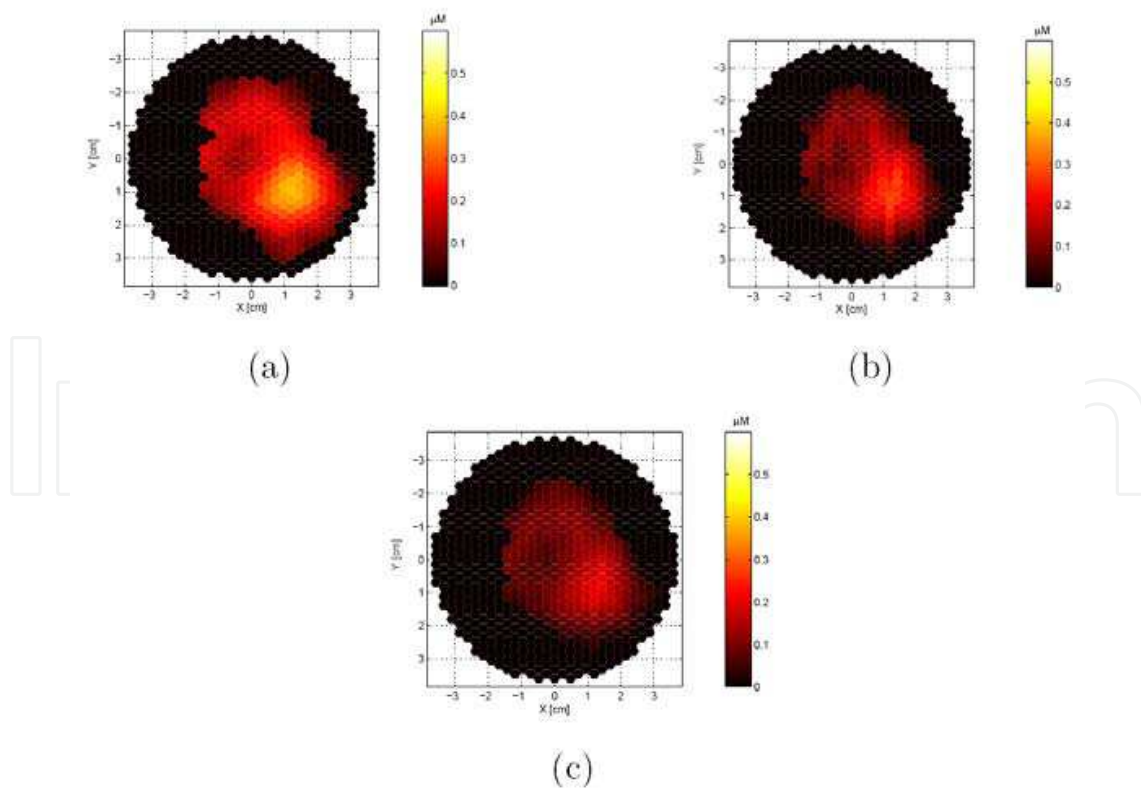

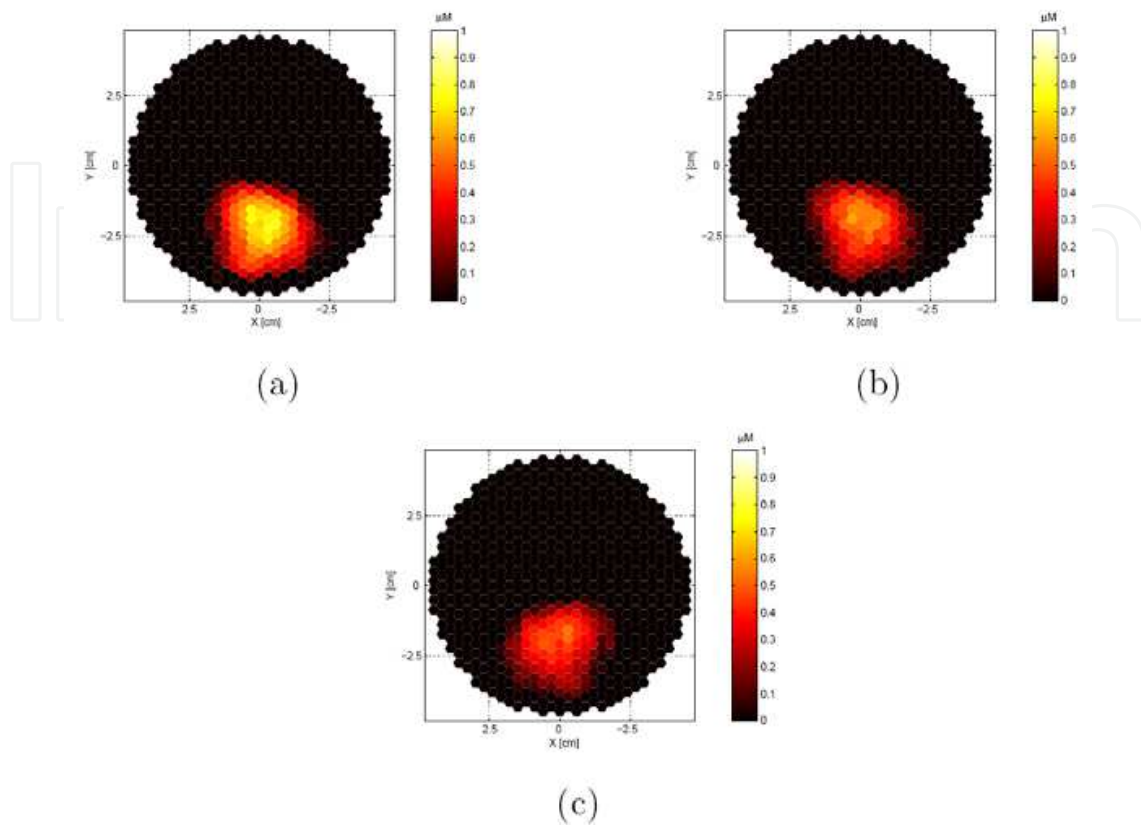Fig. 15. ICG concentration images in plasma for Case 3 for (a) 246.4th, (b) 378.4th, and (c) 510.4th seconds.

Fig. 16. ICG concentration images in plasma for Case 3 for (a) 246.4th, (b) 378.4th, and (c) 510.4th seconds.

7. References

Akaike, H. (1980). *Likelihood and the Bayes Procedure*, Bayesian Statistics, Univ. Press, Valencia, Spain

Alacam, B.; Yazici B.; Intes, X. & Chance, B. (2006). Extended Kalman filtering for the modeling and analysis of ICG pharmacokinetics in cancerous tumors using NIR optical methods. *Trans. IEEE Biomed. Eng.,* Vol. 53, pp. 1861–1871

Alacam, B.; Yazici, B.; Intes, X.; Chance, B.; & Nokia S. (2008). Pharmacokinetic-rate Images of Indocyanine Green for Breast Tumors using Near Infrared Optical Methods. *Physics in Medicine and Biology*, Vol. 53, No: 4, pp. 837-859

Anderson, D. H. (1983). *Lecture Notes in Biomathematics*: *Compartmental Modeling and Tracer Kinetics*, Springer-Verlag, Berlin

Arridge, S. R. (1999). Optical tomography in medical imaging. *Inverse Prob.,* Vol. 15, pp. 41–93

Becker, A.; Schneider, G.; Riefke, B.; Licha, K. & Semmler W. (1999). Localization of near-infrared contrast agents in tumors by intravital microscopy, *Proc. SPIE,* Vol. 3568, pp. 112-118

Extended Kalman Filtering for the Modeling and Estimation of ICG Pharmacokinetics
in Cancerous Tumors using NIR Measurements

201

Bevilacqua, F.; Berger, A. J.; Cerussi, A. E.; Jakubowski, D. & Tromberg B. J. (2000). Broadband absorption spectroscopy in turbid media by combined frequency-domain and steady-state methods. *Appl. Opt.*, Vol. 39, pp. 6498-6507

Boas, D.; Gaudette, T. & Arridge, S. (2001a). Simultaneous imaging and optode calibration with diffuse optical tomography. *Opt. Exp.* Vol. 8 pp. 263–270

Boas, D.; Brooks, D.; Miller, E.; DiMarzio, C.; Kilmer, M. & Gaudette, R. (2001b). Imaging the body with diffuse optical tomography. *IEEE Signal Proc Magazine*, Vol. 18, pp. 57-74

Boutayeb, M.; Rafaralahy, H. & Darouach M. (1997). Convergence analysis of the Extended Kalman Filter used as an observer for nonlinear deterministic discrete-time systems. *IEEE Transactions on Automatic Control*, Vol. 42 No. 4, pp. 581-586

Box, G. E. P.; Jenkins, G. M. & Reinsel G.C. (1994). *Time Series Analysis: Forecasting and Control*, Third edition, Prentice Hall, New York

Buckley, D. L. (2002). Uncertainty in the analysis of tracer kinetics using dynamic contrast-enhanced T1-weighted MRI. *Magn. Reson. Med.*, Vol. 47, pp. 601-606

Catlin, C. E. (1989). *Estimation, Control, and the Discrete Kalman Filter*, Springer, New York

Chen, C. (1999). *Linear System Theory and Design*, Oxford University Press, New York

Chen, Y.; Liu, Q.; Huang, P.; Hyman, S.; Intes, X.; Lee, W. & Chance, B. (2003). Assessment of tumor angiogenesis using fluorescence contrast agents, *Proc. of the SPIE*, Vol. 5254 No. 1, pp. 296-301

Chui, C.K. & Chen, G. (1999). *Kalman Filtering with real time applications*, Springer, Berlin, 1999

Cobelli, C.; Foster, D. & Toffolo G. (2000). *Tracer Kinetics in Biomedical Research: from Data to Model*, Kluwer Academic/Plenum, New York

Cuccia, D.J.; Bevilacqua, F.; Durkin, A. J.; Merritt, S.; Tromberg, B. J.; Gulsen, G.; Yu, H.; Wang, J. & Nalcioglu O. (2003). In vivo quantification of optical contrast agent dynamics in rat tumors by use of diffuse optical spectroscopy with magnetic resonance imaging coregistration. *Applied Optics*, Vol. 42, No. 1, pp. 2940-2950

El Deosky, A.; Seifalian, A.; Cope, M.; Delpy, D. & Davidson B. (1999). Experimental study of liver dysfunction evaluated by direct Indocyanine green clearance using near infrared spectroscopy. *Br. J. Surg.*, Vol. 86, pp. 1005-1011

Fishkin, J. B.; Coquoz, O.; Anderson, E.; Brenner, M. & Tromberg B. J. (1997). Frequency-domain photon migration measurements of normal and malignant tissue optical properties in a human subject. *Appl. Opt.*, Vol. 36, pp. 10-20

Furukawa, K.; Crean, D. H.; Mang, T. S.; Kato, H. & Dougherty T. J. (1995). Fluorescence detection of premalignant, malignant, and micrometastatic disease using hexylpyropheophorbide, *Proc. SPIE,* Vol. 2371, pp. 510-514.

Gelb, A. (1989). *Applied Optimal Estimation*, M.I.T. Press, Cambridge

Gurfinkel, M.; Thompson, A. B.; Ralston, W.; Troy, T. L.; Moore, A. L.; Moore, T. A.; Gust, J. D.; Tatman, D.; Reynolds, J. S.; Muggenburg Nikula, B.K.; Pandey, R.; Mayer, R. H.;

Hawrysz, D. J. & Sevick-Muraca E. M. (2000). Pharmacokinetics of ICG and HPPH-car for the detection of normal and tumor tissue using fluorescence, near-infrared reflectance imaging: a case study. *Photochem Photobiol.*, Vol. 72, pp. 94-102

Hansen, D.; Spence, A.; Carski, T. & Berger M. (1993). ICG staining and demarcation of tumor margins in a rat glioma model. *Surg. Neurol*, Vol. 40, pp. 451-456.

Hansen, P. & O'Leary, D. (1993). The use of the *L*-curve in the regularization of discrete ill-posed problems. *SIAM J. Sci. Comput.* Vol. 14, pp. 1487–1503

Harvey, A. (1993). *Time Series Models*, MIT Press

Hawrys, D. & Sevick-Muraca, E. (2000). Developments toward diagnostic breast cancer imaging using Near-Infrared optical measurements and fluorescent contrast agents. *Neoplasia*, Vol. 2, pp. 388-417

Intes, X..; Ripoll, J.; Chen, Y.; Nioka, S.; Yodh, A. G. & Chance, B. (2003). Continuous-wave optical breast imaging enhanced with Indocyanine Green. *Med. Phys*, Vol. 30-6, pp.1039-1047

Intes, X. & Chance, B. (2005). Non-PET functional imaging techniques: optical.. *Radio. Clin. North Am.* Vol.43., pp.221-234

Jacquez, J. A. (1972). *Compartmental Analysis in Biology and Medicine: Kinetics of Distribution of Tracer-labeled Materials*, Elsevier Pub. Co., New York

Jakubowski, D. J. (2002). *Development of broadband quantitative tissue optical spectroscopy for the non-invasive characterization of breast disease,* Beckman Laser Institute, University of California, Irvine

La Scala, B. F. & Bitmead, R. R. (March 1996). Design of an extended Kalman filter frequency tracer. *IEEE Tran. On Sig. Proc.*, Vol. 44, No. 3, pp. 739-742

Landsman, M. L. J.; Kwant, G.; Mook, G. A. & Zijlstra, W. G. (1976). Light-absorbing properties, stability, and spectral stabilization of indocyanine green. *J. Appl. Physiol.*, Vol. 40, pp. 575–583

Li, X.; Beauvoit, B.; White, R.; Nioka, S.; Chance, B. & Yodh, A. (1995). Tumor localization using fluorescence of ICG in rat models, *Proc. SPIE*, Vol. 2389, pp. 789-797

Ljung, L. (1979). Asymptotic Behavior of the Extended Kalman Filter as a Parameter Estimator for Linear Systems. *IEEE Tran. Automa. Cont.*, Vol. AC-24-1, pp. 36-50

Merritt, S.; Bevilacqua, F.; Durkin, A. J.; Cuccia, D. J.; Lanning, R.; Tromberg, B. J.; Gulsen, G.; Yu, H.; Wang, J. & Nalcioglu O. (2003). Monitoring tumor physiology using near-infrared spectroscopy and MRI coregistration. *Appl. Opt.*, Vol. 42, pp. 2951-2959

Milstein, A. B.; Webb, K. J. & Bouman, C. A., (2005). Estimation of kinetic model parameters in fluorescence optical diffusion tomography *J. Opt. Soc. Am,*. Vol. 22, pp. 1357-1368

Nelson, L. & Stear, E. (1976). The Simultaneous On-Line Estimation of Parameters and States in Linear Systems. *IEEE Tran. on Auto. Control*, Vol.21, pp. 94-98.

Nioka, S.; Yung, Y.; Schnall, M.; Zhao, S.; Orel, S.; Xie, C.; Chance, B. & Solin, S. (1997) .Optical imaging of breast tumor by means of continuous waves. *Adv. Exp. Med. Biol.* Vol. 411, pp. 227–232

Extended Kalman Filtering for the Modeling and Estimation of ICG Pharmacokinetics
in Cancerous Tumors using NIR Measurements
203

Ntziachristos, V.; Chance, B. & Yodh, A. (1999). Differential diffuse optical tomography, *Opt. Exp*. Vol. pp. 5230–5242

Ntziachristos, V.; Yodh, A. G.; Schnall, M. & Chance, B., (2000). Concurrent MRI and diffuse optical tomography of breast after indocyanine green enhancement. *Med. Sci.*, Vol. 97, pp. 2767–2772

O'Leary, M. (1996). Imaging with diffuse photon density waves, *PhD Thesis,* Department of Physics & Astronomy, University of Pennsylvania

Ripoll, J.; Ntziachristos, V.; Carminati, R. & Nieto-Vesperinas, M. (2001a). Kirchhoff approximation for diffusive waves. *Phys. Rev.,* Vol. 64, pp. 051917

Ripoll, J.; Ntziachristos, V.; Culver, J. P.; Pattanayak, D. N.; Yodh, A. G. & Nieto-Vesperinas, M. (2001b). Recovery of optical parameters in multiplelayered diffusive media: theory and experiments. *J. Opt. Soc. Am.*, Vol. 18, pp. 821–830

Sallas, W.M. & Harville, D.A. (1998). *Noninformative Priors and Restricted Maximum Likelihood Estimation in the Kalman Filter.* in J.C. Spall (Ed.), *Bayesian Analysis of Time Series and Dynamic Models*, New York: Marcel-Dekker, Inc.

Schwarz, G. (1978). Estimating the dimensions of a model. *Annals. of Stat.*, Vol. 6, pp. 461-464

Shinohara, H.; Tanaka, A.; Kitai, T.; Yanabu, N.; Inomoto, T.; Satoh, S.; Hatano, E.; Yamaoka, Y. & Hirao, K. (1996). Direct measurement of hepatic indocyanine green clearance with near-infrared spectroscopy: separate evaluation of uptake and removal. *Hepatology*, Vol. 23, pp. 137-144

Su, M. Y.; Muhler, A.; Lao, X. & Nalcioglu, O. (1998). Tumor characterization with dynamic contrast-enhanced MRI using MR contrast agents of various molecular weights. *Magn. Reson. Med.*, Vol. 39, pp. 259-269

Tofts, P. S. (1997). Modeling tracer kinetics in dynamic Gd-DTPA MR imaging. *J. Magn Reson. Imag.*, Vol. 7, pp. 91-101

Tofts. P. S.; Phil, D.; Brix, G.; Buckley, D. L.; Evelhoch, J. L.; Henderson, E.; Knopp, M. V.; Larsson, H. B. W.; Lee, T.; Mayr, N. A.; Parker, G. J. M.; Port, R. E.; Taylor, J. & Weisskoff, R. M. (1999). Estimating Kinetic Parameters From Dynamic Contrast-Enhanced T1-Weighted MRI of a Diffusable Tracer: Standardized Quantities and Symbols. *Jour. Mag. Res. Ima*, Vol. 10, pp. 223-232

Togneri, R. & Deng, L. (2003). Joint State and Parameter Estimation for a Target-Directed Nonlinear Dynamic System Model. *IEEE Tran. on Sig. Proc.,* Vol. 51, No. 12, pp. 3061-3070

Tornoe C. W. (2002). *Grey-Box PK/PD Modeling of Insulin*, M.S. Thesis

Vaupel, P.; Schlenger, K.; Knoop, C. & Hockel, M. (1991). Oxygenation of human tumors: evaluation of tissue oxygen distribution in breast cancers by computerized O2 tension measurements. *Cancer Res.*, Vol. 51, pp. 3316–3322

Yates, M. S.; Bowmer, C. J. & Emmerson, J. (1983). The plasma clearance of indocyanine green in rats with acute renal failure: effect of dose and route of administration. *Biochem. Pharmacol*, Vol. 32, pp. 3109-3114

Yodh, A. & Chance, B. (1995). Spectroscopy and imaging with diffusing light. *Phys. Today,*Vol. 48. No. 3, pp. 34-40

Zarchan, P. (2000). *Fundamentals of Kalman Filtering: a Practical Approach*, American Institute
of Aeronautics and Astronautics, Reston

Kalman Filter Recent Advances and Applications

Edited by Victor M. Moreno and Alberto Pigazo

The aim of this book is to provide an overview of recent developments in Kalman filter theory and their applications in engineering and scientific fields. The book is divided into 24 chapters and organized in five blocks corresponding to recent advances in Kalman filtering theory, applications in medical and biological sciences, tracking and positioning systems, electrical engineering and, finally, industrial processes and communication networks.

How to reference

In order to correctly reference this scholarly work, feel free to copy and paste the following:

INTECH
open science | open minds